Ultrasmall Iridium Nanoparticles as Efficient Peroxidase Mimics for Colorimetric Bioassays

Zheng Xi,[†,#] Weiwei Gao,[†,#] Alexander Biby,[†] Arden Floyd,[†] and Xiaohu Xia[†,‡,*]

[†]Department of Chemistry, and [‡]NanoScience Technology Center, University of Central Florida, Orlando, Florida 32816, United States

ABSTRACT: In this work, we report a peroxidase mimic composed of iridium (Ir) nanoparticles with an average size of only 1.1 nm that are coupled to a tungsten suboxide ($WO_{2.72}$) nanorod as support. Such a peroxidase mimic exhibited an area-specific catalytic efficiency as high as 1.5×10^4 s^{-1} nm^{-2}, outperforming most existing peroxidase mimics of noble metals. As proof-of-concept demonstrations, the peroxidase mimic was applied to colorimetric immunoassays of carcinoembryonic antigen (a cancer biomarker) and aflatoxin B1 (a potent carcinogen), which provided substantially enhanced detection sensitivities compared to conventional enzyme-based assays.

KEYWORDS: *Peroxidase mimics • iridium nanoparticle • particle size • catalysis • bioassay*

Recently, peroxidase mimics made of noble-metal (e.g., Pt, Pd, Ir or Ru) nanomaterials have drawn great attention owning to their distinct advantages relative to natural peroxidases, such as enhanced stabilities and superior catalytic efficiencies.[1] They have been actively applied to many fields in biomedicine, including biosensing, imaging and therapy.[1,2] Significantly, their catalytic efficiency – a critical parameter that largely determines their performance in certain bio-application – can be tuned and optimized by carefully controlling the physicochemical parameters (e.g., size, shape, elemental composition, and crystal structure).[3]

In conventional heterogeneous catalysis, maneuvering the size of a noble-metal nanocatalyst has been proven to be a highly effective approach to improve its catalytic activity.[4] In many cases, ultrasmall nanoparticles (NPs), typically with sizes of a couple or even sub-nanometers, tend to possess better catalytic activities because of the more dominant low-coordinated atoms on NP surface.[5] For instance, Pt NPs of 0.9 nm deposited on electrode was reported to display ~2.5 and 13 times higher specific catalytic activities towards electrochemical oxygen reduction reaction than Pt NPs of 1.2 nm and 2.5 nm, respectively.[6] Nevertheless, in most bio-applications, NPs are desired to be well dispersible in aqueous solution.[7] Therefore, development and utilization of ultrasmall noble-metal NPs as peroxides mimics in bio-applications are extremely difficult because they tend to aggregate in aqueous solution owing to the high surface energy.[8] To our knowledge, noble-metal peroxidase mimics with sizes of a few nanometers or smaller were rarely reported. Taken together, it is worthwhile yet challenging to explore noble-metal NPs of ultrasmall sizes as peroxidase mimics for bio-applications.

Herein, we report a facile one-pot synthesis of ultrasmall Ir NPs coupled to $WO_{2.72}$ nanorods (NRs) as peroxidase mimics, which are termed "Ir/$WO_{2.72}$ nanocomposites (NCs)" in following discussion. Those Ir NPs had an average size of only 1.1 nm (composed of less than 50 Ir atoms).[9] In our design, $WO_{2.72}$ NR was chosen as support for Ir NPs because it can: i) circumvent the aforementioned NP aggregation issue owing to its high hydrophilicity;[10] and ii) amplify the signal from catalysis by assembling multiple Ir NPs on a single NR. Owing to the ultrasmall size of Ir NPs, the Ir/$WO_{2.72}$ NCs displayed an area-specific peroxidase-like catalytic efficiency as high as 1.5×10^4 s^{-1} nm^{-2}, outperforming most previously reported noble-metal peroxidase mimics. Moreover, the surface of Ir/$WO_{2.72}$ NCs are capped with citrate, allowing for convenient conjugation of biomolecules (e.g., antibodies) through attractive electrostatic interactions between citrate and antibodies.[11,12] As proof-of-concept demonstrations, the Ir/$WO_{2.72}$ NCs were applied to immunoassays of carcinoembryonic antigen (CEA, a cancer biomarker[13]) and aflatoxin B1 (AFB1, a carcinogenic toxin[14]), which achieved much lower limits of detection compared to conventional horseradish peroxidase (HRP) based assays.

In a typical synthesis of Ir/$WO_{2.72}$ NCs, WCl_4 and Na_3IrCl_6 as precursors were dissolved in ethanol simultaneously in the presence of sodium citrate (Na_3CA). The solution was transferred to a teflon-lined stainless-steal autoclave and heated to 180 °C for 24 h (Figure 1A). Experimental details are provided in Supporting Information. Figure 1B and Figure S1 show the typical transmission electron microscopy (TEM) images of the Ir/$WO_{2.72}$ NCs. The Ir/$WO_{2.72}$ NCs tended to align side by side on TEM grid due to the intrinsic rich oxygen vacancies and defects of $WO_{2.72}$ NRs that led to strong interactions with each other,[15] while they could disperse well in aqueous solution owing to their highly hydrophilic surfaces (see the inset photograph in Figure 1B). From the high-angle annular dark-field scanning TEM (HAADF-STEM) image shown in Figure 1C, the ultrasmall Ir NPs on $WO_{2.72}$ NRs surface can be observed due to the brighter image contrast of Ir relative to $WO_{2.72}$. Significantly, no obvious aggregation of Ir NPs were found. The size of the Ir NPs was measured to be 1.1 ± 0.4 nm from the magnified STEM image (Figure 1D). The atomic ratio of elemental Ir to W (Ir/W) in the NCs was determined to be 20.44% by inductively coupled plasma mass spectroscopy

(ICP-MS) analysis, which is close to the ratio of Ir and W precursors initially added to the synthesis (i.e., 20%). The high-resolution STEM image in Figure 1E and Figure S2 clearly show two sets of lattice fringe spacing: 0.37 nm from the (010) plane of monoclinic $WO_{2.72}$ NRs;[16] and 0.21 nm from the (111) plane of face-centered cubic (fcc) Ir NPs.[17] The energy-dispersive X-ray spectroscopy (EDS) analyses, including the elemental mapping images (Figure 1F) and line-scan profiles (Figure 1G), further confirmed that Ir NPs were distributed across the $WO_{2.72}$ NR surfaces without obvious aggregations.

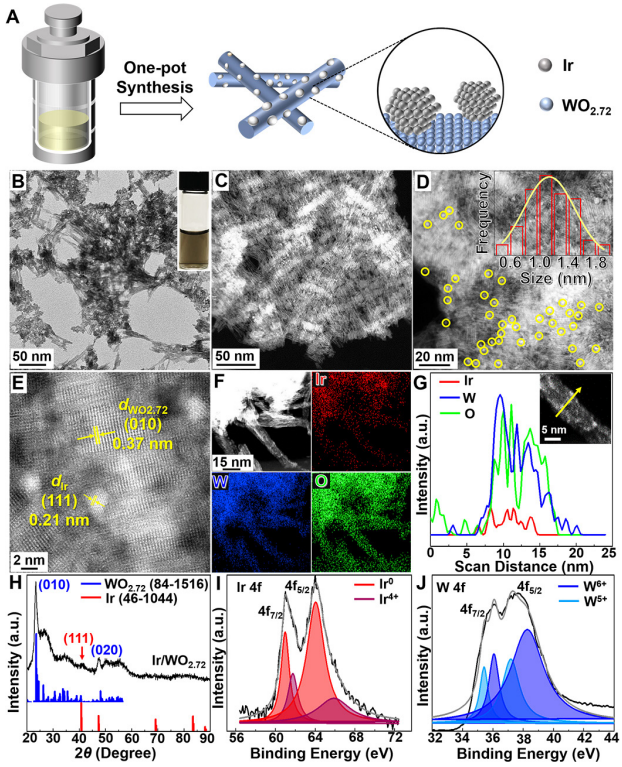

Figure 1. Synthesis and characterizations of Ir/$WO_{2.72}$ NCs with Ir/W atomic ratio ≈ 20%. (A) Schematics showing the synthetic method; (B) TEM image, along with a photograph of aqueous suspension of Ir/$WO_{2.72}$ NCs (inset); (C) HAADF-STEM image; (D) magnified HAADF-STEM. Yellow circles highlight the regions containing Ir NPs; (E) High-resolution STEM image; (F) EDS elemental mapping; (G) EDS line-scan profiles recorded from the arrow direction in inset; (H) XRD pattern; (I) XPS Ir 4f spectra; (J) XPS W 4f spectra.

The X-ray diffraction (XRD) pattern of the Ir/$WO_{2.72}$ NCs (Figure 1H) clearly demonstrated the monoclinic structure of $WO_{2.72}$ ($P_{2/m}$, JCPDS 84-1516). A relatively weak and broad Ir(111) peak was observed, implying the small size of Ir NPs. The Ir/$WO_{2.72}$ NCs were also analyzed by X-ray photoelectron spectroscopy (XPS, see Figures S3, 1I and 1J). Ir in the sample was mostly in metallic state (Ir^0), with the co-existence of a small portion of Ir^{4+}, presumably caused by the surface Ir atoms coordinated with surfactant (Figure 1I)[18]. W element existed in both W^{5+} and W^{6+} (Figure 1J), suggesting the abundant oxygen defects on $WO_{2.72}$ NR surfaces.[15] The fourier transform infrared (FT-IR) spectroscopy of the Ir/$WO_{2.72}$ NCs (Figure S4) shows the characteristic bands from C=O stretch (~1610 cm^{-1}), as well as a wide band from the O-H stretch (3300-3500 cm^{-1}), suggesting the presence of Na_3CA on the surfaces.[19] All these characterization results demonstrated the successful synthesis of Ir/$WO_{2.72}$ NCs that composed of ultrasmall Ir NPs deposited on $WO_{2.72}$ NRs with Na_3CA on the surface.

It is worth mentioning that the atomic ratio of elemental Ir to W (Ir/W) in the Ir/$WO_{2.72}$ NCs can be conveniently controlled by simply varying the amount of Ir precursor in a synthesis (see Supporting Information for details). As examples, Ir/$WO_{2.72}$ NCs with Ir/W of ~10% and ~30% were obtained (see Figure S5 for TEM images of both samples). Their elemental compositions were confirmed by ICP-MS (see Table S1). As shown in Figure S6, Ir NP sizes of all the three samples were similar (*i.e.*, in the range of 1.1-1.3 nm). It should be noted that when the loading amount of Ir was increased to Ir/W ≈ 30%, Ir NPs in the sample tended to aggregate (Figure S5B). Interestingly, if no W precursor was added to the synthesis, significant aggregation of Ir NPs occurred (Figure S7A); while if no Ir precursor was added, $WO_{2.72}$ NRs could still be obtained with a similar morphology to those NRs shown in Figure 1 (see Figure S7B). These results suggest the significance of $WO_{2.72}$ NRs in preventing the ultrasmall Ir NPs from aggregation.

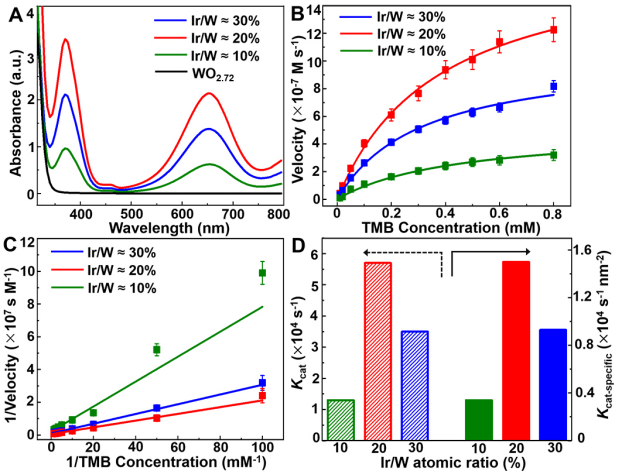

Figure 2. Peroxidase-like catalytic efficiencies of Ir/$WO_{2.72}$ NCs with different Ir/W atomic ratios. (A) UV-vis spectra recorded from different catalysts-mediated reaction solutions at t = 1 min. The amount of Ir was kept the same for all Ir/$WO_{2.72}$ NCs. The amount of pristine $WO_{2.72}$ NRs was the same as that of Ir/$WO_{2.72}$ NCs with Ir/W ≈ 20%; (B) Michaelis–Menten curves; (C) Fitted double-reciprocal plots generated from (B); (D) Histograms comparing K_{cat} and $K_{cat\text{-}specific}$ values of Ir NPs in Ir/$WO_{2.72}$ NCs of different Ir/W ratios. Error bars in (B, C) indicate standard deviations of three independent measurements.

Peroxidase-like catalytic activities of the Ir/$WO_{2.72}$ NCs were evaluated through the oxidation of 3,3',5,5'-tetramethylbenzidine (TMB, a classic substrate of peroxidase[20]) by H_2O_2 as a model reaction. This catalytic reaction yields a blue-colored oxidation product with λ_{max} = 653 nm (i.e., oxTMB) that can be monitored through a UV-vis spectrophotometer.[20] Figure 2A compares the UV-vis spectra recorded from reaction solutions catalyzed by three different Ir/$WO_{2.72}$ NCs with various Ir/W ratios, as well as pristine $WO_{2.72}$ NRs. The results demonstrated that Ir/$WO_{2.72}$ NCs with Ir/W ≈ 20% displayed the highest catalytic activity. It should be pointed out that pristine $WO_{2.72}$ NRs could barely catalyze

the reaction. Moreover, if the $WO_{2.72}$ NRs were selectively etched away from the Ir/$WO_{2.72}$ NCs, Ir NP agglomerates were obtained (Figure S8). The Ir NP agglomerates displayed peroxidase-like catalytic activity (Figure S9). These results demonstrated that Ir NPs were the catalytic active centers of Ir/$WO_{2.72}$ NCs. The relatively low catalytic activities of Ir/$WO_{2.72}$ NCs with Ir/W ≈ 10% and 30% might be ascribed to the sparseness and aggregation of catalytic active centers, respectively.[21]

To quantify the catalytic efficiencies of Ir NPs on those three different Ir/$WO_{2.72}$ NCs, the apparent steady-state kinetic assay was performed (see Supporting Information for details).[22] Typical Michaelis−Menten curves (Figure 2B) and corresponding fitted double-reciprocal plots (Figure 2C) for the Ir/$WO_{2.72}$ NCs were obtained. From these curves and plots, various kinetic parameters of Ir NPs were derived and summarized in Table S1. As a key parameter, the catalytic constant (K_{cat}, defined as the maximum number of substrate conversions per second per catalyst[22]) that measures the catalytic efficiency was highlighted in Figure 2D. Ir NPs on Ir/$WO_{2.72}$ NCs with Ir/W ≈ 20% showed the highest K_{cat} value of 5.7×10^4 s^{-1}. Significantly, area-specific efficiency ($K_{cat\text{-}specific}$, defined as normalized K_{cat} to the surface area of an individual catalyst[22]) of these Ir NPs was determined to be as high as 1.5×10^4 s^{-1} nm^{-2}. To the best of our knowledge, these ultrasmall Ir NPs exhibited the highest area-specific efficiency among all reported peroxidase mimics of noble metals. As shown by Table S2, the $K_{cat\text{-}specific}$ values of other noble-metal peroxidase mimics are up to the regime of 10^3 s^{-1} nm^{-2}.

To demonstrate potential bio-applications of the Ir/$WO_{2.72}$ NCs, we applied them to bioassays. Colorimetric enzyme-linked immunosorbent assay (ELISA, a widely used bioassay technology[23-25]) was chosen as a model platform. The Ir/$WO_{2.72}$ NCs with Ir/W ≈ 20% (sample in Figure 1) that possess maximized catalytic efficiency were used as labels. To assess the generality and versatility of the Ir/$WO_{2.72}$ NCs-based ELISA (Ir/$WO_{2.72}$ ELISA), we applied it to two different and general assay formats – "sandwich mode" and "competitive mode".[26] In both ELISAs, the Ir/$WO_{2.72}$ NCs are conjugated to secondary antibodies and act as peroxidase mimics to specifically generate color signal by catalyzing the oxidation of TMB by H_2O_2.[27] The intensities of color signal in the "sandwich" and "competitive" ELISAs, respectively, are directly and inversely proportional to the amount of analyts present in the sample.[23] For comparison, the Ir/$WO_{2.72}$ ELISA was benchmarked against conventional horseradish peroxidase-based ELISA (HRP ELISA), where the same set of antibodies were used in both ELISAs. It is worth noting that the Ir/$WO_{2.72}$-goat anti-mouse IgG conjugates can be conveniently prepared by simply mixing Ir/$WO_{2.72}$ NCs and IgG in phosphate-buffered saline (PBS) buffer.[12] Details about assembly and procedures of these ELISAs are provided in the Supporting Information.

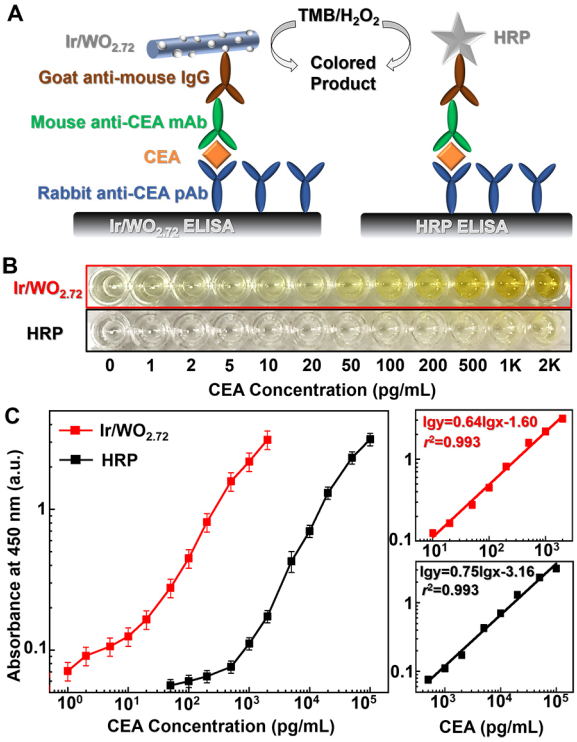

Figure 3. Ir/$WO_{2.72}$ NC- and HRP-based ELISAs of CEA in a "sandwich mode". (A) Schematics of both ELISAs. (B) Photographs of the ELISAs of CEA standards. (C) Calibration curves (left) and linear range regions (right) of the detection results in (B). Error bars indicate standard deviations of eight independent measurements.

In "sandwich ELISA" (Figure 3A), carcinoembryonic antigen (CEA, a cancer biomarker[13]) as a model analyte was detected. CEA standards of different concentrations were analyzed in microtiter plate wells (Figure 3B), where the catalytic reaction of TMB and H_2O_2 was quenched by H_2SO_4 to yield yellow-colored product (i.e., diimine, λ_{max} = 450 nm[20]) that can be quantified by a microplate reader. Figure 3C compares the calibration curves of both Ir/$WO_{2.72}$ and HRP ELISAs of CEA. The Ir/$WO_{2.72}$ ELISA displayed a linear detection range of 10-2000 pg/mL with low coefficients of variation in 2.3%−8.7%. Limit of detection (LOD, defined the CEA concentration corresponding to a signal that is three times the standard deviation above the zero calibrator[28]) of the Ir/$WO_{2.72}$ ELISA was determined to be 2.2 pg/mL based on its calibration curve, which is 174-fold lower than that of HRP ELISA (382 pg/mL). Such a significantly enhanced detection sensitivity of the Ir/$WO_{2.72}$ ELISA could be ascribed to the high catalytic efficiency of ultrasmall Ir NPs that were well dispersed on $WO_{2.72}$ NRs. To support this argument, we also tested the Ir agglomerates obtained from $WO_{2.72}$ NRs etched away from the Ir/$WO_{2.72}$ NCs (Figure S8), and they provided a lower detection sensitivity when applied to ELISA of CEA (Figure S10). Notably, the Ir/$WO_{2.72}$ ELISA demonstrated good stabilities, in addition to high sensitivity. No obvious change of detection signal across all CEA concentrations was observed for the Ir/$WO_{2.72}$ ELISA during the period of 21-day storage (see Figure S11). These results imply that either Ir was not further oxidized during the 21-day storage, or the oxidation of Ir NPs did not influence their performance in bioassay.

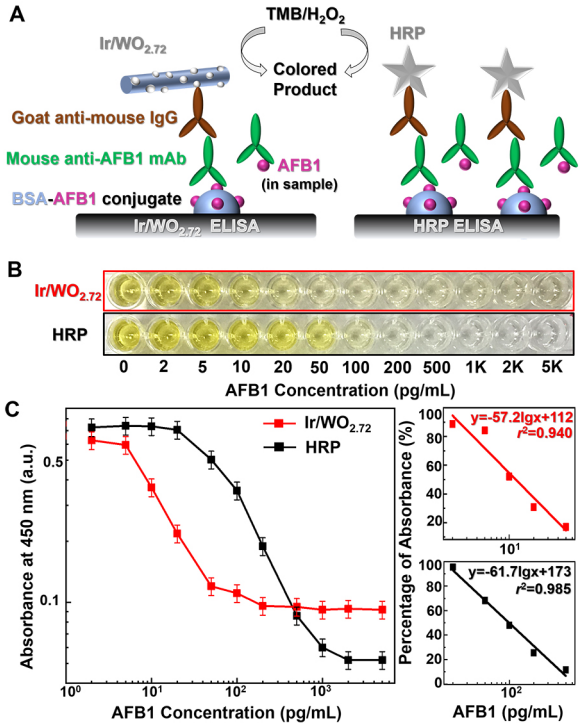

Figure 4. Ir/$WO_{2.72}$ NC- and HRP-based ELISAs of AFB1 in a "competitive mode". (A) Schematics of both ELISAs. BSA: bovine serum albumin. (B) Photographs of the ELISAs of AFB1 standards. (C) Calibration curves (left) and linear range regions (right) of the detection results in (B). Error bars indicate standard deviations of eight independent measurements.

In "competitive ELISA" (Figure 4A), aflatoxin B1 (AFB1, a potent carcinogen in contaminated foods produced by certain molds[14]) as a model analyte was assayed. Unlike the "sandwich ELISA", in this type of ELISA, AFB1 in sample compete with a reference (i.e., BSA-AFB1 conjugate) for binding to a limited amount of antibody.[29] The intensity of color signal is inversely proportional to the amount of AFB1 in samples. AFB1 standards of various concentrations were analyzed by both the Ir/$WO_{2.72}$ and HRP ELISAs (Figure 4B). Figure 4C compares the calibration curves of both ELISAs of AFB1. The Ir/$WO_{2.72}$ ELISA displayed a linear detection range of 2-50 pg/mL with low coefficients of variation in 3.6%–8.5%. The LOD (defined as the AFB1 concentration corresponding to a signal that is 90% of the negative control[30]) for Ir/$WO_{2.72}$ ELISA was determined to be 2.3 pg/mL, which is 10-folds lower than that of HRP ELISA. It should be mentioned that, compared to Ir/$WO_{2.72}$ ELISA, HRP ELISA required five times more usage amounts of BSA-AFB1 conjugates and detection antibodies in order to ensure similar color signal at negative controls for both ELISAs. If such usage amounts were kept the same, HRP ELISA would provide much lower detection sensitivity (see Figure S12). Similar to Ir/$WO_{2.72}$ ELISA of CEA, the performance Ir/$WO_{2.72}$ ELISA of AFB1 was compromised when $WO_{2.72}$ was removed from the Ir/$WO_{2.72}$ NCs (Figure S13). As shown by Figure S14, the Ir/$WO_{2.72}$ ELISA of AFB1 also showed good stabilities.

In summary, we have demonstrated a type of highly efficient and versatile peroxidase mimic – ultrasmall Ir NPs (1.1 nm in size) deposited on $WO_{2.72}$ nanorods. The ultrasmall Ir NPs possess an area-specific catalytic efficiency as high as 1.5 $\times 10^4$ s^{-1} nm^{-2}, outperforming most already reported peroxidase mimics of noble metals. The Ir NPs-based mimics were applied to immunoassays of CEA (a cancer biomarker) and AFB1 (a potent carcinogen) that showed substantially enhanced detection sensitivities compared to conventional natural peroxidase-based assays.

ASSOCIATED CONTENT

Supporting Information.

The Supporting Information is available free of charge via the Internet at http://pubs.acs.org.

Experimental details including chemicals, materials, instrumentation, and synthesis, discussion of peroxidase-like activity, ELISA of CEA and AFB1, XPS survey spectra, FT-IR spectra, TEM images, ELISA stability results, comparison of catalyst kinetic parameters and efficiencies, additional refs

AUTHOR INFORMATION

Corresponding Author

*Xiaohu Xia − *Department of Chemistry and Nanoscience Technology Center, University of Central Florida, Orlando, Florida 32816, United States*; Email: Xiaohu.Xia@ucf.edu

Author Contributions

#Z. X. and W. G. contributed equally to this work.

Notes

The authors declare no competing financial interest.

ACKNOWLEDGMENT

This work was supported in part by the grants from the National Science Foundation (CBET-1804525 and CHE-1834874) and the startup funds from University of Central Florida (UCF).

REFERENCES

(1) Wu, J.; Wang, X.; Wang, Q.; Lou, Z.; Li, S.; Zhu, Y.; Qin, L.; Wei, H. Nanomaterials with Enzyme-like Characteristics (Nanozymes): Next-Generation Artificial Enzymes (II). *Chem. Soc. Rev.* **2019**, *48*, 1004-1076.

(2) Liang, M.; Yan, X. Nanozymes: From New Concepts, Mechanisms, and Standards to Applications. *Acc. Chem. Res.* **2019**, *52*, 2190-2200.

(3) Wei, Z.; Xi, Z.; Vlasov, S.; Ayala, J.; Xia, X. Nanocrystals of Platinum-Group Metals as Peroxidase Mimics for *in vitro* Diagnostics. *Chem. Commun.* **2020**, *56*, 14962-14975.

(4) Cao, S.; Tao, F.; Tang, Y.; Li, Y.; Yu, J. Size- and Shape-Dependent Catalytic Performances of Oxidation and Reduction Reactions on Nanocatalysts. *Chem. Soc. Rev.* **2016**, *45*, 4747-4765.

(5) Nesselberger, M.; Roefzaad, M.; Hamou, R. F.; Biedermann, P. U.; Schweinberger, F. F.; Kunz, S.; Schloegl, K.; Wiberg, G. K. H.; Ashton, S.; Heiz, U.; Mayrhofer, K. J. J.; Arenz, M. The Effect of Particle Proximity on the Oxygen Reduction Rate of Size-Selected Platinum Clusters. *Nat. Mater.* **2013**, *12*, 919-924.

(6) Yamamoto, K.; Imaoka, T.; Chun, W.; Enoki, O.; Katoh, H.; Takenaga,M.; Sonoi, A. Size-Specific Catalytic Activity of Platinum Clusters Enhances Oxygen Reduction Reactions. *Nat. Chem.* **2009**, *1*, 397-402.

(7) Liu, Y.; Purich, D. L.; Wu, C.; Wu, Y.; Chen, T.; Cui, C.; Zhang, L.; Cansiz, S.; Hou, W.; Wang, Y.; Yang, S.; Tan, W. Ionic Functionalization of Hydrophobic Colloidal Nanoparticles to Form Ionic Nanoparticles with Enzymelike Properties. *J. Am. Chem. Soc.* **2015**, *137*, 14952-14958.

(8) Shrestha, S.; Wang, B.; Dutta, P. Nanoparticle Processing: Understanding and Controlling Aggregation. *Adv. Colloid Interface Sci.* **2020**, *279*, 102162.

(9) Yamamoto, H.; Maity, P.; Takahata, R.; Yamazoe, S.; Koyasu, K.; Kurashige, W.; Negishi, Y.; Tsukuda, T. Monodisperse Iridium Clusters Protected by Phenylacetylene: Implication for Size-Dependent Evolution of Binding Sites. *J. Phys. Chem. C* **2017**, *121,* 10936-10941.

(10) Guo, C.; Yin, S.; Yan, M.; Kobayashi, M.; Kakihana, M.; Sato, T. Morphology-Controlled Synthesis of $W_{18}O_{49}$ Nanostructures and Their Near-Infrared Absorption Properties. *Inorg. Chem.* **2012**, *51*, 4763-4771.

(11) Lin, H.; Liu, Y.; Huo, J.; Zhang, A.; Pan, Y.; Bai, H.; Jiao, Z.; Fang, T.; Wang, X.; Cai, Y.; Wang, Q.; Zhang, Y.; Qian, X. Modified Enzyme-Linked Immunosorbent Assay Strategy Using Graphene Oxide Sheets and Gold Nanoparticles Functionalized with Different Antibody Types. *Anal. Chem.* **2013**, *85*, 6228-6232.

(12) Glomm, W. R.; Halskau, O., Jr.; Hanneseth, A. M.; Volden, S. Adsorption Behaviour of Acidic and Basic Proteins onto Citrate-coated Au Surfaces Correlated to Their Native Fold, Stability, and pI. *J. Phys. Chem. B* **2007**, *111*, 14329-14345.

(13) Benchimol, S.; Fuks, A.; Jothy, S.; Beauchemin, N.; Shirota, K.; Stanners, C. P. Carcinoembryonic Antigen, a Human-Tumor Marker, Functions as an Intercellular-Adhesion Molecule. *Cell* **1989**, *57*, 327-334.

(14) Massey, T. E.; Stewart, R. K.; Daniels, J. M.; Liu, L. Biochemical and Molecular Aspects of Mammalian Susceptibility to Aflatoxin B1 Carcinogenicity. *Proc. Soc. Exp. Biol. Med.* **1995**, *208*, 213-227.

(15) Xi, G.; Ouyang, S.; Li, P.; Ye, J.; Ma, Q.; Su, N.; Bai, H.; Wang, C. Ultrathin $W_{18}O_{49}$ Nanowires with Diameters Below 1 nm: Synthesis, Near-infrared Absorption, Photoluminescence, and Photochemical Reduction of Carbon Dioxide. *Angew. Chem. Int. Ed.* **2012**, *51*, 2395-2399.

(16) Xi, Z.; Erdosy, D. P.; Mendoza-Garcia, A.; Duchesne, P. N.; Li, J.; Muzzio, M.; Li, Q.; Zhang, P.; Sun, S. Pd Nanoparticles Coupled to $WO_{2.72}$ Nanorods for Enhanced Electrochemical Oxidation of Formic Acid. *Nano Lett.* **2017**, *17*, 2727-2731.

(17) Pi, Y.; Zhang, N.; Guo, S.; Guo, J.; Huang, X. Ultrathin Laminar Ir Superstructure as Highly Efficient Oxygen Evolution Electrocatalyst in Broad pH Range. *Nano Lett.* **2016**, *16*, 4424-4430.

(18) Jin, G.; Liu, J.; Wang, C.; Gu, W.; Ran, G.; Liu, B.; Song, Q. Ir Nanoparticles with Multi-enzyme Activities and Its Application in the Selective Oxidation of Aromatic Alcohols. *Appl. Catal. B Environ.* **2020**, *267*, 118725.

(19) Bai, Z.; Yang, L.; Zhang, J.; Li, L.; Hu, C.; Lv, J.; Guo, Y. High-Efficiency Carbon-Supported Platinum Catalysts Stabilized with Sodium Citrate for Methanol Oxidation. *J Power Sources* **2010**, *195*, 2653-2658.

(20) Josephy, P. D.; Eling, T. E.; Mason, R. P. The Horseradish Peroxidase-Catalyzed Oxidation of 3,5,3′,5′ Tetramethylbenzidine. Free Radical and Charge-Transfer Complex Intermediates. *J. Biol. Chem.* **1982**, *257*, 3669-3675.

(21) Xia, C.; Qiu, Y.; Xia, Y.; Zhu, P.; King, G.; Zhang, X.; Wu, Z.; Kim, J. Y.; Cullen, D. A.; Zheng, D.; Li, P.; Shakouri, M.; Heredia, E.; Cui, P.; Alshareef, H. N.; Hu, Y.; Wang, H. General Synthesis of Single-atom Catalysts with High Metal Loading Using Graphene Quantum Dots. *Nat. Chem.* **2021**, *13*, 887-894.

(22) Xia, X.; Zhang, J.; Lu, N.; Kim, M. J.; Ghale, K.; Xu, Y.; McKenzie, E.; Liu, J.; Ye, H. Pd-Ir Core-Shell Nanocubes: A Type of Highly Efficient and Versatile Peroxidase Mimic. *ACS Nano* **2015**, *9*, 9994-10004.

(23) Lequin, R. M. Enzyme Immunoassay (EIA)/Enzyme-Linked Immunosorbent Assay (ELISA). *Clin. Chem.* **2005**, *51*, 2415-2418.

(24) Liu, P.; Han, L.; Wang, F.; Li, X.; Petrenko, V. A.; Liu, A. Sensitive Colorimetric Immunoassay of Vibrio Parahaemolyticus Based on Specific Nonapeptide Probe Screening from a Phage Display Library Conjugated with MnO_2 Nanosheets with Peroxidase-like Activity. *Nanoscale* **2018**, *10*, 2825-2833.

(25) Liu, P.; Wang, Y.; Han, L.; Cai, Y.; Ren, H.; Ma, T.; Li, X.; Petrenko, V. A.; Liu, A. Colorimetric Assay of Bacterial Pathogens Based on Co_3O_4 Magnetic Nanozymes Conjugated with Specific Fusion Phage Proteins and Magnetophoretic Chromatography. *ACS Appl Mater Interfaces* **2020**, *12*, 9090-9097.

(26) Kumada, Y.; Katoh, S.; Imartaka, H.; Imamura, K.; Nakanishi, K. Development of a One-Step ELISA Method Using an Affinity Peptide Tag Specific to a Hydrophilic Polystyrene Surface. *J. Biotechnol.* **2007**, *127*, 288-299.

(27) Xi, Z.; Wei, K.; Wang, Q.; Kim, M. J.; Sun, S.; Fung, V.; Xia, X. Nickel-Platinum Nanoparticles as Peroxidase Mimics with a Record High Catalytic Efficiency. *J. Am. Chem. Soc.* **2021**, *143*, 2660-2664.

(28) Armbruster, D. A.; Tillman, M. D.; Hubbs, L. M. Limit of Detection (LQD)/Limit of Quantitation (LOQ): Comparison of the Empirical and the Statistical Methods Exemplified with GC-MS Assays of Abused Drugs. *Clin. Chem.* **1994**, *40*, 1233-1238.

(29) Kohl, T. O.; Ascoli, C. A. *Cold Spring Harbor Protocols*, **2017**, DOI: 10.1101/pdb.prot093757.

(30) Xia, X.; Xu, Y.; Ke, R.; Zhang, H.; Zou, M.; Yang, W.; Li, Q. A Highly Sensitive Europium Nanoparticle-based Lateral Flow Immunoassay for Detection of Chloramphenicol Residue. *Anal. Bioanal. Chem.* **2013**, *405*, 7541-7544.

Entry for the Table of Contents

A highly efficient peroxidase mimic composed of ultrasmall Ir nanoparticles (1.1 nm in size) coupled to a $WO_{2.72}$ nanorod was developed. The mimic was successfully applied to colorimetric bioassays, which provided much higher detection sensitivities compared to conventional enzyme-based assays.